Atypical Defect Motions in Brittle Layered Sodium Titanate Nanowires

Arixin Bo, [†,1] Kai Chen, [‡,1] Edmund Pickering,[†] Haifei Zhan,[†] John Bell,[†] Aijun Du,[†] Yongqiang Zhang,[†] Xiaoguang Wang,[†] Huaiyong Zhu,[†] Zhiwei Shan[‡,*] and Yuantong Gu[†,*]

[†]School of Chemistry, Physics and Mechanical Engineering, Queensland University of Technology, 2 George Street, Brisbane, Queensland 4000, Australia.

[‡]Center for Advancing Materials Performance from the Nanoscale (CAMP-Nano) & Hysitron Applied Research Center in China (HARCC), State Key Laboratory for Mechanical Behavior of Materials, Xi'an Jiaotong University, Xi'an, Shaanxi 710049, China

[1] These authors contributed equally to this work.

Abstract

In situ tensile tests show atypical defect motions in the brittle $Na_2Ti_3O_7$ (NTO) nanowire (NW) within the elastic deformation range. After brittle fracture, elastic recovery of the NTO NW is followed by reversible motion of the defects in a time-dependent manner. *In situ* cyclic loading-unloading test shows that these mobile defects shift back and forth along the NW in accordance with the loading-unloading cycles and eventually restore their initial
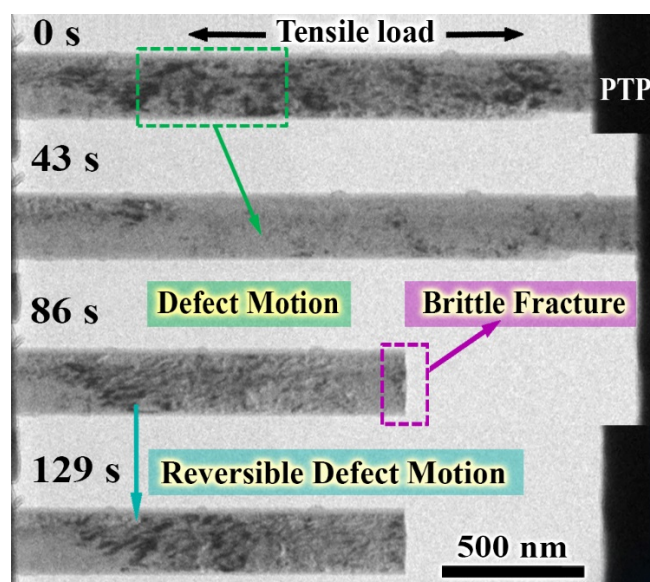
positions after the load is completely removed. The Exsistence of the defects within the NTO NWs and their motions do not lead to plastic deformation of the NW. The atypical defect motion is speculated to be the result of glidibility of the TiO_6 layers where weakly bonded cation layers are inbetween. Exploration of the above novel observation can establish new understandings of the deformation behavior of superlattice nanostructures.

Defect motion is considered exclusively as the driving mechanism for ductile deformation in crystalline materials. In comparison, material brittle deformation and defects migration is generally uncorrelated at low temperatures. With the continuous exploration of nanomaterials, observations that are contradictory to the knowledge of conventional material deformation are not uncommon. As the materials shrink down to the nanoscale, peculiar mechanical behaviors unattainable to their bulky counterparts are observed,[1-3] such as superplasticity,[4,5] bending anelasticity[6], and atypical strain hardening[7]. Defects are believed to be greatly responsible to these phenomena. Currently, nanoscale deformation investigations are mostly focusing on materials with relatively simple structures like metals, binary semiconductors and simple metal oxides.[8-10] In these systems, dislocation actively participate in the deformation process as suggested by numerous experimental, numerical, and theoretical investigations.[11-14] In comparison, the deformation behaviors and the role of defects are still unclear for the superlattice materials, which are crystals with specifically oriented sub-molecular nanolayers.[15] Since defects presenting in such anisotropic layered structures could affect the deformation behavior, mechanical investigation can provide interesting and essential insights to the structure-defect relation and actively drives the development of such nanomaterials.

In the family of layered inorganic structures, sodium titanates ($Na_2Ti_3O_7$ abbreviated as NTO) have been attracting continuous attention, primarily in Na-ion batteries,[16] bio-related structural materials in terms of scaffolding[17] and other applications in waste water treatment[18] and photocatalyst.[19] Like many alkali titanates, covalently bonded TiO_6 octahedral structures in NTO are linked to form negatively charged zigzag ribbons with exchangeable layers of Na^+ cations between the TiO_6 layers where Coulombic forces hold the different layers together.[20] Different synthetic processes can generate various NTO morphologies like NWs, nanotubes, nanolaminae, and NW arrays.[21-24] Possessing large aspect ratio and surface area, these low dimensional NTO structures are crucial to their applications. To accommodate the applications of such versatile material, mechanical characterization of the strength and stability of the one dimensional (1D) NTO nanostructure is required. From three-point bending tests, NTO NWs are shown to possess a brittle characteristic like silicon.[25] On the other hand, silicon NWs have been reported to show large-strain plasticity (LSP) under uniaxial deformation at room temperature,[26] due to the emergence of dislocations followed by lattice distortion and amorphization. Thus it is involuntary to ask if the 1D NTO nanostructures also demonstrate LSP.

2

Tensile investigations on the 1D nanomaterials have been widely conducted using micro-electromechanical system (MEMS) devices which focus on metallic NWs, e.g. Si,[27] Ag,[28] Ni,[29] Au,[30] Pd,[31] binary oxide NWs, e.g. ZnO,[32] VO$_2$,[33] and alloy Ge$_2$Sb$_2$Te$_5$[34] materials. The technique has been proven to be useful to obtain information on both mechanical properties and inherent deformation pathways of the nanomaterials. In this work, we used a MEMS based push-to-pull (PTP) device inside a transmission electron microscope (TEM) to investigate the tensile behavior of NTO NW, enabling simultaneous measurement of both stress-strain relations and microstructure evolution during deformation. Under tensile loading, NTO NWs consistently fracture in a brittle manner while significant defect movement, which is generally assigned to ductile deformation, is observed at the same time. After the NW fractures (external loading being released), detection of a reversal defect motion is confirmed within the materials and the process happens in a time-dependent manner. Lastly, cyclic tensile testing shows a repeatable elastic modulus measurement under each cycle while defects are observed to move back-and-forth during load-unload process.

Single crystalline NTO NWs with P2$_1$/m space group are synthesized using a hydrothermal method.[25] Detailed X-ray diffraction (XRD) and Raman spectroscopy analysis can be found in Figure S1 and S2 of the Supplementary Materials. TEM images show that the NTO NWs possess high length-to-width ratio (in excess of 30) and uniform lateral dimensions (Figure 1(a)). The NW width ranges from 20-700 nm and the observed maximum NW length is around 40 μm. The high resolution TEM (HRTEM) image in Figure 1(b) shows that (100) plane has a *d*-spacing of 0.93 nm and is parallel to the NW longitudinal direction. One-thrid of (001) plane has a measured *d*-spacing of 0.36 nm and is oriented at 77° with respect to (100) plane. Both *d*-spacings and the angle between them are in good accordance with the reported structure and XRD data. These observations are confirmed from the indexed selected area electron diffraction (SAED) pattern shown in the Figure 1(c), which is also consistent with the fast Fourier transform (FFT) image (Figure 1(b) inset) derived from the HRTEM image. A comprehensive crystalline structural model of NTO NW (Figure 1(d)), independent from TEM characterizations, is built using Visualization for Electronic and Structural Analysis (VESTA) software. The 3D crystalline structure is based on structural information from XRD analysis which can be matched with the TEM results. The (100) and (001) planes are marked by the red dash lines as shown in top image of Figure 1(d), which is viewed along [010] crystal direction. It can be seen from the molecular model that the parallel pair

of TiO$_6$ zigzag ribbons (highlighted in Figure 1(d) top image) orients at an angle with the (100) plane i.e. crystallographic direction [001] or NW longitudinal direction. Rotating the 3D structure along the NW longitudinal direction, the crystalline orientation with respect to the overall longitudinal direction of the NW is shown in Figure 1(d), bottom image.

Contrasts are commonly visible in the NTO NWs under both bright field and dark field TEM imaging modes, as displayed in Figure 1(e), due to the electron scattering on lattice defects. A close resemblance of such contrast and defects are reported on irradiated Ag NWs.[35] HRTEM analysis on the NTO NW shows wide but inhomogeneous distributions of various types of materials defects as seen in Figure 1(f-h). Specifically, in Figure 1(f), a series of dislocations are highlighted and pointed out by the black arrows. Lattice distortions implying the existence of defects can be observed on the right among which one of them is highlighted. In Figure (g), the red marker highlights the formation of twining with the twin boundary being parallel to the (100) planes as well as other notable dislocations. In addition, several dislocations are presented in Figure 1(h) as marked. Notably, such widely distributed defects are formed during the hydrothermal synthesis of NTO NWs, and thus they exist without any external loading conditions. No amorphous layer is detected on NTO surfaces regardless of NW sizes from HRTEM images. The observed nanoscale surface roughness may potentially serve as stress concentrators.[36]
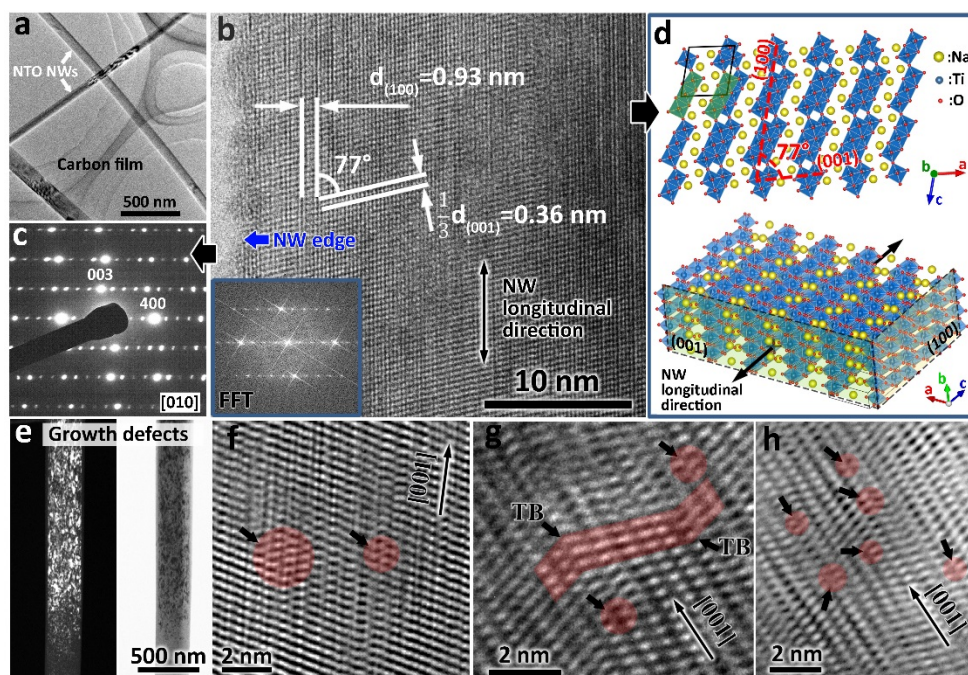

Figure 1. Structural characterization of NTO NW. (a) TEM image showing individual NTO NWs dispersed on a carbon grid film. (b) HRTEM image taken at the edge of a NTO NW. *d*-spacings of the identified plane

are marked in the graph in which case $d_{(100)}$=0.93 nm and 1/3 of $d_{(001)}$=0.36 nm.. FFT image of the crystalline structure is shown in the inset. (c) Indexed electron diffraction pattern taken from the NTO NW sample in (b). (d) Model of NTO crystalline structure constructed by VESTA using data from XRD analysis. In the top figure, the black box shows the unit cell under [010] viewing direction. (e) Dark and bright field TEM images showing the contrast spots which indicate the growth defects of NTO NW. (f) HRTEM image showing dislocations and lattice distortion on (001) planes. (g) HRTEM image of material defects including dislocations and twinning where twin boundaries (TB) are indicated, highlighted by the red markers and arrows. (h) HRTEM image depicting various dislocations as marked by the red circles.

In situ tensile tests on NTO NWs are conducted with a PI95 TEM Picoindenter, which allow real-time visualization and precise control over the displacement and load.[33, 37] For NW tensile measurements, individual specimens are fixed at the center of a push-to-pull (PTP) device by focused ion beam induced Pt deposition (Figure 2(a)). Compressive force at the circular end of the PTP results in tensile elongation of the NW. Meanwhile, stress induced microstructure evolution is realized through observing the NW across the trench with TEM. It is noteworthy that the Pt deposition at the both ends of the NW is strong enough to avoid breaking-off or gliding of the fixed points which is confirmed by SEM observatioins after the tensile tests.

During the tensile test, a clear observation of NW elongation is depicted in Figure 2(b). The elastic deformation of the NTO NW can be seen by the position changes of the markers as pointed out by the red arrows. The length between the two arrows (a stable feature pointed on the left and a bumpy marker on the NW as pointed on the right side) is elongated as the NW is strained for 2.2% (right before it fractures at 43s). A drastic dynamic change of the growth defects is observed in a way that the defects shift and fade along the NW as it is being stretched. As presented in Figure 2(b) and Movie S1 from the supplementary information, dramatic movement of defects, indicated by the contrast movement, appeared throughout the NW during tensile deformation. Upon fracture (44s), half of the NW to the right side springs away due to the vibrations generated during the sudden mechanical failure. The fractured point shows a uniform squared shape without any sign of necking, indicating the brittle nature of the NWs (which is also well indicated by the stress-strain curve discussed later in Sec. 2.4). The marker position returned to its original position before tensile deformation almost instantly, and the TEM image shows minimal amount of visible defects (cleared dark contrast). Interestingly, continuous observation of the fractured NW shows a reversibly moving defects in a time-dependent manner over the next 1.5 min or so. It should be

noted that, prior to the tensile loading, the defects in the NTO NWs are stationary under electron beam irradiation.
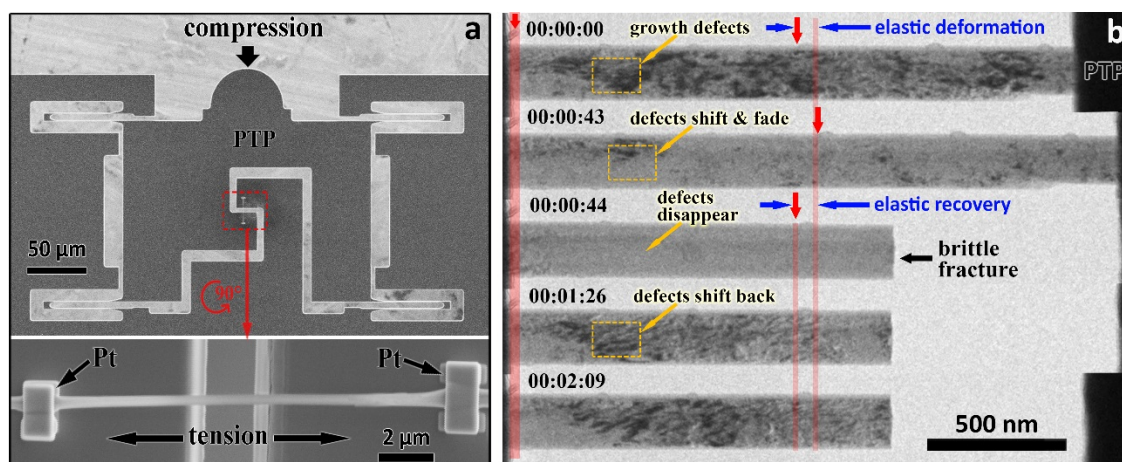

Figure 2. *In situ* tensile setup and the tensile behavior of NTO NWs (a) Scanning electron microscopy (SEM) image of a PTP device on which a NTO NW is fixed across the trench at the center. The bottom image shows a magnified SEM image (rotated 90° from the top image) of the fixed NW. Compression loading at the circular end of the PTP converts to tensile loading at the center. (b) Reversible defect motion of a NTO NW recorded under *in situ* TEM tensile test. TEM images of the NTO NW extracted from an *in situ* tensile test movie. Elastic deformation is depicted by the position change of the bump markers on the sample pointed by red arrows on images. The migration of the defects before and after NW fracture is described by the yellow boxes.

To the best of our knowledge, such a time-dependent defects motion in a brittle 1D nanostructure after fracture is not reported. Factors governing TEM contrast differences such as uneven material thickness and compositional variation can be ruled out since these features cannot move independently under room-temperature tensile deformation. It is commonly acknowledged that, under TEM imaging, altering the incident beam direction (spread/reduce the beam or changing sample position) will result in different visualization condition over the material defects and thus generate a visual sense of "defect shift". However, our observation of defect related contrast change is contradictory to the above case and can be assigned to the defects motion. As shown in Figure 3, when the tensile stress is loaded onto the NW, the top end moves upward while the bottom end stays still. Defects shift is observed during elastic deformation (0-57s), and fracture occurs at 58s. After fracture, the PTP still moves and thus the top end of the NW moves upward

together from 58-63s. From 63-80s, the NW travels downward as the gap between the PTP shrinks as the pushing force imposed onto the PTP is unloaded. From 58-80s, the contrasts on the upper cantilevered NW continuously shift downwards. The speed of contrast shift is also notably different from the traveling speed of the fractured NW. Regarding this, a clear observation of the whole dynamic deformation process can be find in Movie S2. It is certain that the contrast shift is completely independent from the traveling path of the NW, i.e. the substrate material. Based on the above observations, the contrast shifting can be exclusively attributed to the defect motion and not caused by the changes in the imaging conditions. Similar to Figure 2(b), contrast shift (58-80s) is clearly seen at the bottom end of the cantilevered NW where the incident beam and the sample position remains constant which further confirms the above conclusion.
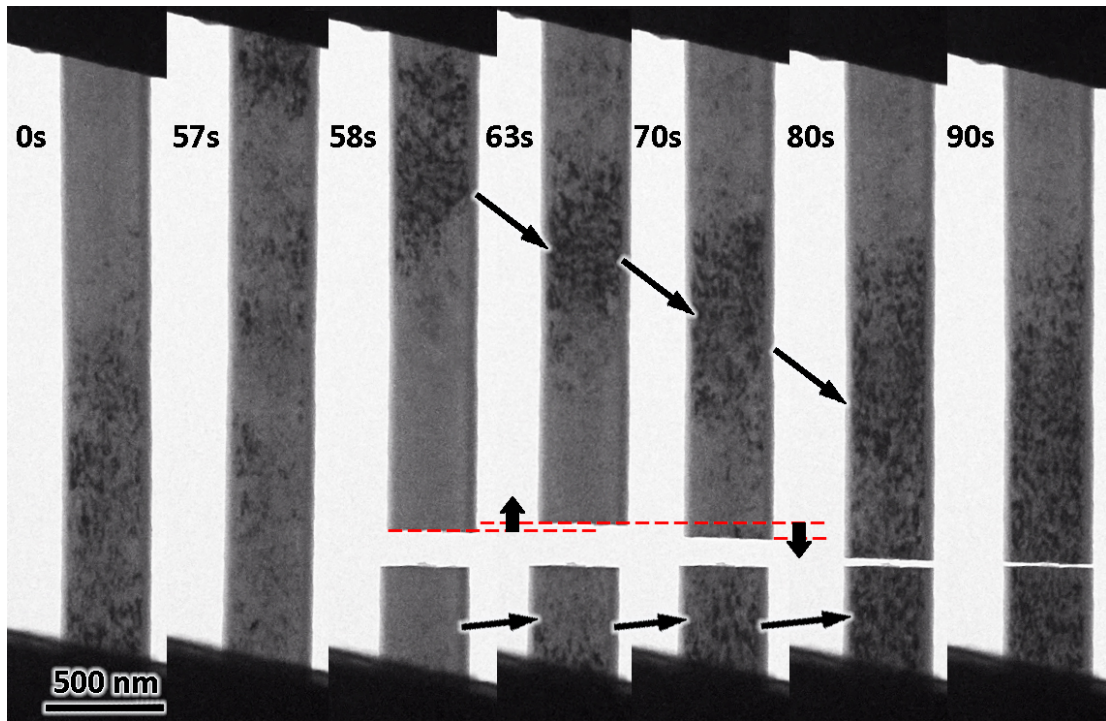

Figure 3. TEM images taken under *in situ* tensile test of a NW showing its defect motion patterns. The images (from left to right) are picked at the time of 0, 57, 58, 70, 80 and 90 seconds during the tensile test.

To examine the relationship between the mechanical responses and the atypical defect motion in NTO NW, further tests are carried out. Primarily, the test environment of *in situ* measurement is inevitable from electron beam irradiation which, to some materials, can alter their mechanical properties.[38] Herein, we examined the mechanical responses of NTO NWs under TEM imaging

conditions with regular imaging condition (low current density). Specifically, a NW is held for a period of time at a specific initial extension, during which the electron beam was shifted away from, and then onto the specimen. During this period, it is found that the mechanical response of the NW remained stable, i.e., the tensile force is stable and independent from the e-beam irradiation state (see Figure S3). This stable mechanical response suggests that the electron beam with the energy and intensity employed in this study do not cause detectable structural and mechanical property change to NTO NWs within the tensile experiment time frame. In a single loading-unloading test shown in Movie S3, defects move along the NTO NW as the tensile loading proceeds (00:05-00:35) while during unloading, these defect patterns shift to their original positions (00:35-00:57, Movie S3). The same reversible defect motion is also recorded under TEM dark field imaging condition (see Movie S4). This phenomenon further suggests the defect motion occurs within the sample and excludes the possibility of changes caused by incident beam or surface contamination.

We also tested the tensile behavior of the NTO NWs under numerous loading-unloading cycles while recording their *f-d* curve for elastic modulus and analysis. As shown in Figure S4, A good match between the NW elongation (derived from measuring the position change of the markers on the NW) and the displacement output from the indenter is confirmed. This indicates a precise calibration of the indenter and ensures an accurate calculation of the tensile strain. Hereafter, the engineering strain is calculated according to $\varepsilon=(L-L_0)/L_0$, with L_0 and L being the initial and elongated length of the NW, respectively. Correspondingly, the engineering stress is derived from $\sigma=F/A$, where F and A represent the tensile force and NW cross-sectional area respectively. The cyclic force function is programmed and the displacement is measured as output. As shown in Figure 4(a), each loading-unloading cycle shows linear deformation curve and the elastic deformation trait is almost identical among the 19 cycles conducted. Young's modulus of NTO NW obtained from the *f-d* curve stays constant during each cycle, and the average value is calculated to be 53 ± 3 GPa (Figure 4(b)). The cyclic tests were repeated on different samples where identical elastic deformation curves are consistently obtained (Figure S5). Along with the reproducible elastic curves, TEM observation depicts the motion of defects is shifting back and forth periodically during the cyclic test. As compared in Figure 4(c), the initial clusters of defects (00:00:00) shift and fade when the NW is elongated (00:00:17) and the elongated state is marked by the blue circle as indicated in Figure 4(a). As the NW is being pulled and released during the

cyclic loading, the defect pattern on the NW is nearly identical at each state under different loading cycles. As illustrated in Figure 4(d) whose loading state is correlated with the yellow markers in the loading state in Figure 4(a), the extracted defect patterns at the elongated state from cyclic tests 2, 3 and 17 (marked by I, II and III) show similar pattern and the defect patterns at their following lowest loading states (marked by α, β and γ) show nearly identical defect patterns. After 19 cycles, the recovered defect cluster is almost the same as its original pattern (Figure 4(c)). It is confirmed from the cyclic loading-unloading test that the defect motion is reversible in the NTO NW under tensile deformation and the defects are able to restore their original positions almost completely. The unchanged electron diffraction patterns before and after loading-unloading process (Figure S6) suggest that the defect motion in NTO NWs is an amorphization free process.
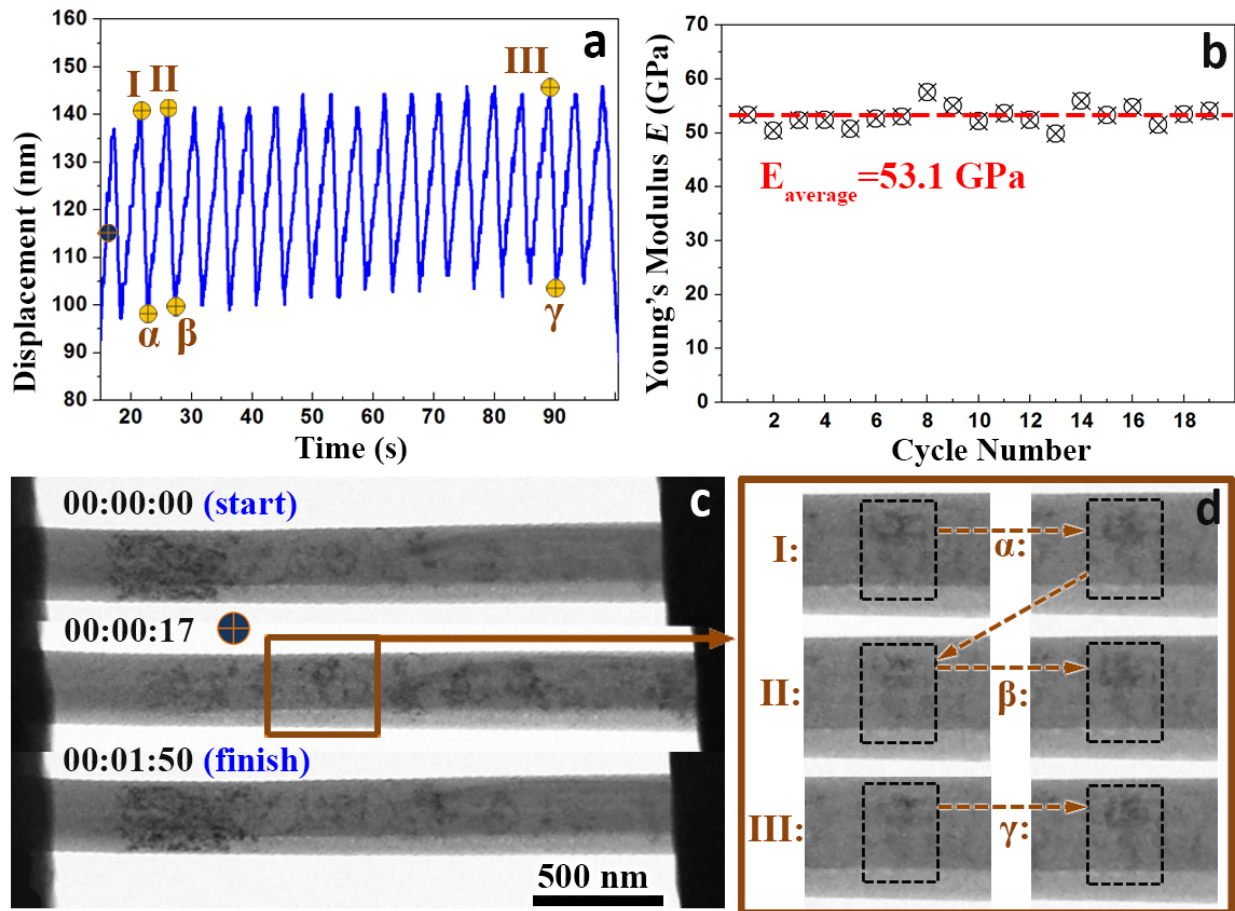

Figure 4. Measurement of elastic deformation of a NTO NW accompanied by reversible defect motion. (a) The displacement vs time as obtained from 19 loading-unloading cyclic *in situ* test on NTO NW. (b) The estimated Young's moduli (E) from each cyclic loading. (c) TEM images from the cyclic loading test showing the initial (00:00:00), elongated (00:00:17), and the final states (00:01:50) of the NTO NW. (d)

Enlarged TEM images showing the defect morphology in a confined region in (c) from cycle number 2, 3 and 17, respectively. It clearly shows that the reversibly mobile defects present nearly identical patterns under the same loading conditions.

Two typical stress-strain curves of NTO NWs are plotted in Figure 5(a) where both show brittle deformation features. The stress increases monotonically (a good linear profile) until reaching a threshold value, after which the stress experiences a sharp reduction to zero. Meanwhile, TEM images (inset in Figure 5(a)) show no cross-section shrinkage or necking which confirms that the NTO NWs experience a brittle fracture under tensile deformation. Such brittle fracture behavior is uniformly observed from the tensile tests for more than 15 samples, despite differences in dimension and initial defect density, which is also in good agreement with the behavior observed under three-point bending test.[25]
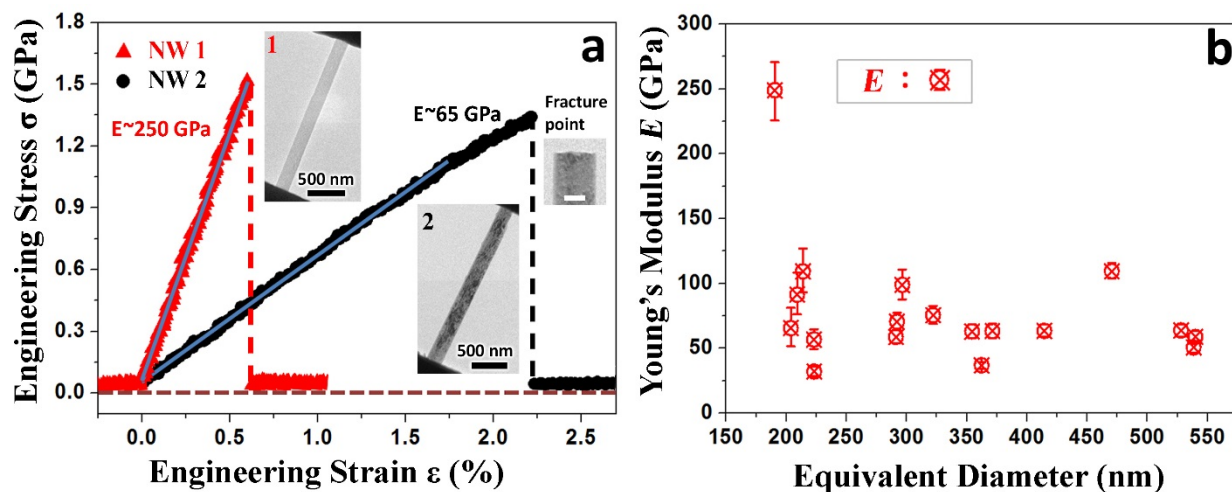

Figure 5. (a) Engineering stress-strain curves of two NWs with similar dimensions (denoted as NW1 and NW2 with a diameter of 180 and 197 nm, respectively). Insets show the TEM images of sample NW1 and 2. The square fracture shape of the NW2 (inset, scale bar 100 nm) is consistently seen in other examined NWs. (b) Estimated Young's modulus (E) of the NTO NWs in relation with their equivalent diameter. Error bars are originated from the differences in sample height measurement using SEM.

A comparison between the measured Young's modulus among all examined NTO NWs is plotted in Figure 5(b), from which a relatively large variance (from 37 GPa to 250 GPa) can be observed. Here, Young's modulus is estimated from the stress-strain curve with the strain within 2% using linear regression. It is found that the estimated Young's modulus fluctuates between 37 GPa to 125 GPa for most of the examined NTO NWs when their equivalent diameter increases

from 200 to ~550 nm, except for the NW with the smallest equivalent diameter. In other words, no clear relationship is found between the Young's modulus and the diameter of the examined NTO NWs. For NWs baring similar diameter (Figure 5a), the difference between the Young's modulus can be significant. It is seen that the "cleaner" NW (NW1 with few initial defects – more uniform and brighter appearance) shows a Young's modulus around 250 GPa. In comparison, NW2 with obvious initial dark contrasts (i.e., initial defects) has a measured Young's modulus of around 65 GPa which is only a quarter of that of NW1 despite their similar equivalent diameter (180 nm for NW1 and 197 nm for NW2, respectively). Such a big variation suggests that the impact on the mechanical properties of NTO NWs arising from their initial defect density cannot be ignored. As demonstrated by experimental and numerical approaches, presence of defects in ceramic materials can alter the chemical bond length and lattice parameters which can result in a significant impact on the elastic modulus.[8,10, 39] The fracture strain of NTO NWs with different equivalent diameter shows a random fluctuation from 0.4% to 2.7% (Figure S7), which is similar to the range of fracture strain for GaN NW[7] but is generally lower than that of ZnO NW (by around 2%).[9]

Having observed the atypical defect motion in brittle NTO NWs, it is confirmed that the load-induced defect motion does not cause notable plastic deformation of the NTO NW. This atypical defect motion is rarely seen on other 1D materials. For example, defect motion in the ceramic SiC NW is non-reversible as the resulting structural amorphization leads to material plasticity.[4] Mo NWs showing initial dislocations exhibit post-yielding plastic deformation which is distinctively different from the dislocation-free samples that only deform elastically.[40] For NTO NWs, it is observed that the defect motion can be initiated at the early stage of elastic deformation. It can be deducted that the energy required to induce the defect motion is greatly lower than the loading energy that causes its final brittle fracture. As mentioned, NTO NW possesses a superlattice structure which is comprised of Na^+ and TiO_6 ribbon layers. Early studies show that the layer of Na^+ can be easily exchanged while the TiO_6 layers do not collapse during ion exchange even in strong alkali or acidic conditions.[41] In other words, NTO NW has stable covalent intra-layer bonding and less stable inter-layer ionic interactions. Numerically, the ability to perform layer gliding has been reported for similar $Na_{0.5}NbS_2$ superlattice possessing defects.[42] Electrochemically, for layered nanostructures, layer gliding and its reversible motion take place as responses to the system energy change.[43] For these superlattices, it is reported that the role of

interlayer cation (Na^+) is to stabilize the layered structures by reducing the electrostatic repulsion between the negatively charged layers. When Na^+ is unbalanced, reversible layer gliding happens.[44] Despite the limitation of precise observation on the defect types during the *in situ* loadings, it is reasonable to relate the defect motion to the Na^+ cations bonded by the weak electrostatic force whereas the fractrure of the NW requires breaking of the covalent Ti-O bonds that needs much higher energy. To confirm the underlying mechanism for this atypical defect motion in NTO NWs, atomistic simulations are favored, where development of an appropriate empirical interatomic potential is needed.

In summary, this work reported an atypical defect motion in the layered NTO NW as carefully observed during the *in situ* tensile deformation. It is found that the NTO NWs consistently deform in a brittle manner whereas the elastic deformation is accompanied by a drastic motion of defects which is generally associated with plastic deformation. Strikingly, after the brittle fracture, defect patterns in the NTO NWs are found to migrate gradually along the NW in a reversible manner. Cyclic loading-unloading *in situ* tensile tests show that the defects shift and fade during loading. After complete unloading, these defects are found to shift back and restore their initial morphologies. Such an abnormal defect motion is likely resulted from the TiO_6 layer gliding facilitated by the weakly bonded Na^+ cations layers in-between. The estimated Young's modulus ranges from 37 to 250 GPa, with the fracture strain varying from 0.4% to 2.7%. It is worth noting that visualization of the individual defect motion under such tensile deformation setup is limited by extremely high stability requirement under high resolution imaging conditions which is hard to realize under mechanical loading conditions. To fill this gap, numerical modelling is a useful technique, but requires appropriate interatomic potential to be established for this family of layered ceramic materials. In all, experimental investigations confirmed that the brittle NTO NWs can undergo a unique reversible defect motion under tensile deformation, which is not seen in other brittle materials. Further exploration of the above novel observation can establish understandings of the deformation behavior of superlattice nanostructures and potentially develop materials in nanoscale lubricant or damping applications.

Methods

Synthesis and characterization. NTO NW preparation procedure is reported and can be found elsewhere.[25] After collecting the NWs, various structural characterizations are conducted. XRD

patterns of the powder sample were recorded on a Philips PANalytical X'pert pro diffract meter equipped with graphite monochromator. Cu Kα radiation and a fixed power source (40 kV and 40 mA) were used. The XRD data were collected over a 2θ range between 3.5˚ and 75˚, at a scanning rate of 2.5˚ min[-1]. The TEM characterization and the HRTEM investigations were carried out on a FEI Tecnai F20 operating at 200 kV. For TEM sample preparation, the specimens were dispersed in ethanol by sonification and deposited onto a copper microgrid coated with holey carbon film. The SEM imaging was carried on Zeiss scanning electron microscopy. Raman spectrum was taken at room temperature using Renishaw inVia Raman Microscope at 785 nm wavelength.

In situ tensile test. Tensile test specimen was prepared in a FEI Helios NanoLab 600i dual-beam Focused ion beam (FIB) system. The NTO NWs are dispersed onto a carbon micro-grid from which they are picked up by a nanomanipulator (Kleindiek GmbH) and secured on the PTP device via electron beam induced Pt deposition (Figure S8 (a)). Both ends of the NW were welded via the focused electron-beam induced Pt deposition (EBID) to firmly fix the NW across the trench. Markers were made on the NW sample by carbon deposition to obtain precise displacement during tension. *In situ* tensile tests were carried out under displacement-control mode using Hysitron PI95 PicoIndenter[45] with a 1×2 μm flat diamond punch in a JEOL2100F TEM operated at 200kV, and the indentation rate was set at 5 nm s^{-1}. Cyclic loading tests are measured by force-control mode. By providing a compressive force to the semicircular end of PTP, a tensile load is generated to the NW at the PTP center (Figure S8 (b), (c)). Real-time imaging can be recorded simultaneously with applying uniaxial tension the NWs (Figure S8 (d)) and the frame rate for the tensile test recording was 10 frames per second.

Tensile data processing. The readout force of the PTP-based tensile test includes force applied to stretch NW and force to expend the PTP trench. To obtain the actual tensile force data on the NW sample, spring constant of the PTP is measured after NW tensile fracture. Then, force applied to the NW can be obtained by subtracting PTP contributed force from the raw force and stress σ can be derived. There is also thermal drift from the Picoindenter and this effect can be effectively corrected by TEM image processing using Matlab. To calculate the engineering strain, the raw displacement data was divided by the initial NW length which was measured during SEM sample preparation as the distance between the two Pt deposition points. After removing the mechanical response of PTP from the recorded force, the engineering stress-strain curve of the NW sample can be obtained. The cross section areas of NTO NWs are found to be rectangular shaped. During

calculation, an equivalent diameter is used which is converted from measured NW width and height via SEM. In other words, the square root of the NW cross section area (NW width × height) is referred as the equivalent diameter. Then the Young's modulus is calculated from the linear part of the loading curve in a stress-strain curve.

Supporting Information

This material is available free of charge via the Internet at http://. Information on XRD patterns, Raman spectrum, *in situ* bending, *in situ* tensile test calibrations, TEM images of defect motion trait, SAED pattern before and after tensile deformation are included.

AUTHOR INFORMATION

Corresponding Authors

*E-mail: zwshan@xjtu.edu.cn

*E-mail: yuantong.gu@qut.edu.au

Author Contributions

A.B., K.C. H.Z. J.B. Z.S. and Y.G designed the research; A.B. and H.Y.Z. synthesized the samples and A.B. performed the X-ray diffraction, Raman spectroscopy characterizations, push-to-pull sample preparations and high resolution TEM imaging; A.B. and E.P. conducted *in situ* tensile tests, data analysis and E.P competed the thermal drift corrections; Y.Z. and X.W. conducted in situ tensile tests on beam effect study and cyclic tests. All the authors participated in the results discussion. A.B., K.C., A.D., Z.S. and Y.G. wrote the paper and all the authors read and commented on the manuscript.

Notes

The authors declare no competing financial interests.

References

(1) Lu, Y.; Huang, J.Y.; Wang, C.; Sun, S.; Lou, J. Cold welding of ultrathin gold nanowires. *Nat. Nanotechnol*. **2010**, *5*, 218.

(2) Chen, B.; Gao, Q., Wang, Y.; Liao, X.; Mai, Y. W.; Tan, H.H.; Zou, J.; Ringer, S. P.; Jagadish, C. Anelastic behavior in GaAs semiconductor nanowires. *Nano Lett*. **2013**, *13*, 3169.

(3) Wu, B.; Heidelberg, A.; Boland, J.J. Mechanical properties of ultrahigh-strength gold nanowires. *Nat. Mater*. **2005**. *4*, 525.

(4) Han, X.D.; Zhang, Y.F.; Zheng, K.; Zhang, X.N.; Zhang, Z.; Hao, Y.J.; Guo, X.Y.; Yuan, J.; Wang, Z.L. Low-temperature in situ large strain plasticity of ceramic SiC nanowires and its atomic-scale mechanism. *Nano Lett*. **2007**, *7*, 452.

(5) Wang, Y.B.; Wang, L.F.; Joyce, H.J.; Gao, Q.; Liao, X.Z.; Mai, Y.W.; Tan, H.H.; Zou, J.; Ringer, S.P.; Gao, H.J.; Jagadish, C. Super Deformability and Young's Modulus of GaAs Nanowires. *Adv. Mater*. **2011**, 23, 1356.

(6) Cheng, G.; Miao, C.; Qin, Q.; Li, J.; Xu, F.; Haftbaradaran, H.; Dickey, E.C.; Gao, H.J.; Zhu, Y. Large anelasticity and associated energy dissipation in single-crystalline nanowires. *Nat. Nanotechnol*. **2015**, *10*, 687.

(7) Shan, Z.W.; Mishra, R.K.; Asif, S.A.S.; Warren, O.L.; Minor, A.M. Mechanical annealing and source-limited deformation in submicrometre-diameter Ni crystals. *Nat. Mater*. **2008**, *7*, 115.

(8) Dai, S.; Zhao, J.; He, M.; Wang, X.; Wan, J.; Shan, Z.; Zhu, J. Elastic properties of GaN nanowires: Revealing the influence of planar defects on Young's modulus at nanoscale. *Nano Lett*. **2014**, *15*, 8.

(9) Agrawal, R.; Peng, B.; Espinosa, H.D. Experimental-computational investigation of ZnO nanowires strength and fracture. *Nano Lett*. **2009**, *9*, 4177.

(10) Wang, X.; Chen, K.; Zhang, Y.; Wan, J.; Warren, O.L.; Oh, J.; Li, J.; Ma, E.; Shan, Z. Growth Conditions Control the Elastic and Electrical Properties of ZnO Nanowires. *Nano Lett*. **2015**, *15*, 7886.

(11) Yamakov, V.; Wolf, D.; Phillpot, S.R.; Gleiter, H. Dislocation–dislocation and dislocation–twin reactions in nanocrystalline Al by molecular dynamics simulation. *Acta Mater*. **2003**, *51*, 4135.

(12) Yu Q.; Qi L.; Chen K.; Mishra R.K.; Li J.; Minor A.M. The Nanostructured Origin of Deformation Twinning. *Nano lett*. **2012**, 12, 887.

(13) Zhang J.; Hao S.; Jiang D.; Huan Y.; Cui L.; Liu Y.; Ren, Y.; Yang H. Dual Phase Synergy Enabled Large Elastic Strains of Nanoinclusions in a Dislocation Slip Matrix Composite. *Nano lett*. **2018**, 18, 2976.

(14) Bao, P.; Wang, Y.B.; Cui, X.; Gao, Q.; Yen, H.W.; Liu, H.; Yeoh, W.K.; Liao, X.; Du, S.; Tan, H.H.; Jagadish, C.; Zou, J.; Ringer, S.P.; Zheng, R. Atomic-scale Observation of Parallel Development of Super Elasticity and Reversible Plasticity in GaAs Nanowires. *Appl. Phys. Lett*. **2014**, 104, 0219041

(15) Pluchino P.A.; Chen X.; Garcia M.; Xiong L.; McDowell D.L.; Chen Y. Dislocation migration across coherent phase interfaces in SiGe superlattices. *Comput. Mater. Sci*. **2016**, 111, 1.

(16) Han, M.H.; Gonzalo, E.; Singh, G.; Rojo, T. A comprehensive review of sodium layered oxides: powerful cathodes for Na-ion batteries. *Energy Environ. Sci*. **2015**, *8*, 81.

(17) Becker, I.; Hofmann, I.; Müller, F.A. Preparation of bioactive sodium titanate ceramics. *J. Eur. Ceram. Soc*. **2007**, *27*, 4547.

(18) Yang, D.J.; Zheng, Z.F.; Zhu, H.Y.; Liu, H.W.; Gao, X.P. Titanate nanofibers as intelligent absorbents for the removal of radioactive ions from water. *Adv. Mater*. **2008**, *20,* 2777.

(19) Parayil, S.K.; Razzaq, A.; Park, S.M.; Kim, H.R.; Grimes, C.A.; In, S.I. Photocatalytic conversion of CO_2 to hydrocarbon fuel using carbon and nitrogen co-doped sodium titanate nanotubes. *Appl. Catal. A* **2015**, 498, 205.

(20) Yakubovich, O.; Kireev, V. Refinement of the crystal structure of $Na_2Ti_3O_7$. *Crystallogr. Rep.* **2003**, *48*, 24.

(21) Yang, D.; Zheng, Z.; Yuan, Y.; Liu, H.; Waclawik, E.R.; Ke, X.; Xie, M.; Zhu, H. Sorption induced structural deformation of sodium hexa-titanate nanofibers and their ability to selectively trap radioactive Ra (II) ions from water. *Phys. Chem. Chem. Phys.* **2010**, *12*, 1271.

(22) Huang, J.; Huang, Z.; Guo, W.; Wang, M.; Cao, Y.; Hong, M. Facile synthesis of titanate nanoflowers by a hydrothermal route. *Cryst. Growth Des.* **2008**, *8*, 2444.

(23) Yang, D.; Sarina, S.; Zhu, H.; Liu, H.; Zheng, Z.; Xie, M.; Smith, S.V.; Komarneni, S. Capture of radioactive cesium and iodide ions from water by using titanate nanofibers and nanotubes. *Angew. Chem. Int. Ed.* **2011**, *50*, 10594.

(24) Choi, M.; Yong, K. A facile strategy to fabricate high-quality single crystalline brookite TiO_2 nanoarrays and their photoelectrochemical properties. *Nanoscale* **2014**, *6*, 13900.

(25) Bo, A.; Zhan, H.; Bell, J.; Zhu, H.; Gu, Y. Mechanical bending properties of sodium titanate ($Na_2Ti_3O_7$) nanowires. *RSC Adv.* **2014**, *4*, 56970.

(26) Han, X.; Zheng, K.; Zhang, Y.F.; Zhang, X.; Zhang, Z.; Wang, Z.L. Low-temperature in situ large-strain plasticity of silicon nanowires. *Adv. Mater.* **2007**, *19*, 2112.

(27) Kushima, A.; Huang, J.Y.; Li, J. Quantitative fracture strength and plasticity measurements of lithiated silicon nanowires by in situ TEM tensile experiments. *ACS Nano* **2012**, *6*, 9425.

(28) Zhu, Y.; Qin, Q.; Xu, F.; Fan, F.; Ding, Y.; Zhang, T.; Wiley, B.J.; Wang, Z.L. Size effects on elasticity, yielding, and fracture of silver nanowires: in situ experiments. *Phys. Rev. B* **2012**, *85*, 045443.

(29) Lu, Y.; Peng, C.; Ganesan, Y.; Huang, J.Y.; Lou, J. Quantitative in situ TEM tensile testing of an individual nickel nanowire *Nanotechnology* **2011**, *22*, 355702.

(30) Sedlmayr, A.; Bitzek, E.; Gianola, D.S.; Richter, G.; Mönig, R.; Kraft, O. Existence of two twinning-mediated plastic deformation modes in Au nanowhiskers. *Acta Mater.* **2012**, *60*, 3985.

(31) Chen, L.Y.; He, M.; Shin, J.; Richter, G.; Gianola, D.S. Measuring surface dislocation nucleation in defect-scarce nanostructures *Nat. Mater*. **2015**, *14*, 707.

(32) Asthana, A.; Momeni, K.; Prasad, A.; Yap, Y.K.; Yassar, R.S. In situ observation of size-scale effects on the mechanical properties of ZnO nanowires. *Nanotechnology* **2011**, *22*, 265712.

(33) Guo, H.; Chen, K.; Oh, Y.; Wang, K.; Dejoie, C.; Syed A.S.A.; Warren, O.L.; Shan, Z.W.; Wu, J.; Minor, A.M. Mechanics and dynamics of the strain-induced M1–M2 structural phase transition in individual VO_2 nanowires. *Nano Lett*. **2011**, *11*, 3207.

(34) Murphy, K.F.; Chen, L.Y.; Gianola, D.S. Effect of organometallic clamp properties on the apparent diversity of tensile response of nanowires. *Nanotechnology*, **2013**, *24*, 235704.

(35) Yu, K.Y.; Bufford, D.; Sun, C.; Liu, Y.; Wang, H.; Kirk, M.A.; Li, M.; Zhang, X. Removal of stacking-fault tetrahedra by twin boundaries in nanotwinned metals. *Nat. Commun*. **2013**, *4*, 1377.

(36) Weinberger, C.R.; Cai, W. Plasticity of metal nanowires. *J. Mater. Chem*. **2012**, *22*, 3277.

(37) Tian, L.; Cheng, Y.Q.; Shan, Z.W.; Li, J.; Wang, C.C.; Han, X.D.; Sun, J.; Ma, E. Approaching the ideal elastic limit of metallic glasses. *Nat. Commun*. **2012**, *3*, 609.

(38) Zheng, K.; Wang, C.; Cheng, Y.Q.; Yue, Y.; Han, X.; Zhang, Z.; Shan, Z.; Mao, S.X.; Ye, M.; Yin, Y. Electron-beam-assisted superplastic shaping of nanoscale amorphous silica. *Nat. Commun*. **2010**, *1*, 24.

(39) Jhi, S.H.; Louie, S.G.; Cohen, M.L.; Ihm, J. Vacancy hardening and softening in transition metal carbides and nitrides. *Phys. Rev. Lett*. **2001**, *86*, 3348.

(40) Chisholm, C.; Bei, H.; Lowry, M.B.; Oh, J.; Asif, S.A.S.; Warren, O.L.; Shan, Z.W.; George, E.P.; Minor, A.M. Dislocation starvation and exhaustion hardening in Mo alloy nanofibers. *Acta Mater*. **2012**, *60*, 2258.

(41) An, Y.; Li, Z.; Xiang, H.; Huang, Y.; Shen, J. First-principle calculations for electronic structure and bonding properties in layered $Na_2Ti_3O_7$ *Open Phys*. **2011**, *9*, 1488.

(42) Liao, Y.; Park, K.S.; Xiao, P.; Henkelman, G.; Li, W.; Goodenough, J.B. Sodium Intercalation Behavior of Layered Na_xNbS_2 ($0 \leq x \leq 1$). *Chem. Mater*. **2013**, *25*, 1699.

(43) Yabuuchi, N.; Kajiyama, M.; Iwatate, J.; Nishikawa, H.; Hitomi, S.; Okuyama, R.; Usui, R.; Yamada, Y.; Komaba, S. P2-type $Na_x[Fe_{1/2}Mn_{1/2}]O_2$ made from earth-abundant elements for rechargeable Na batteries. *Nat. Mater.* **2012**, *11*, 512.

(44) Lee, E.; Lee, W.C.; Asl, N.M.; Kim, D.; Slater, M.; Johnson, C.; Kim, Y. Reversible $NaVS_2$ (de) intercalation cathode for Na-ion batteries. *ECS Electrochem. Lett.* **2012**, *1*, A71.

(45) Warren, O.L.; Asif, S.A.S.; Cyrankowski, E.; Kounev, K. *Actuatable Capacitive Transducer for Quantitative Nanoindentation Combined with Transmission Electron Microscopy*. U.S. Patent US20070180924 A1, Aug 9, **2007**.